A Diagnostic Study of the Indian Ocean Dipole Mode in El Nino and Non-El Nino Years

Hae-Kyung Lee Drbohlav, Silvio Gualdi, and Antonio Navarra
Istituto Nazionale di Geofisical e Vulcanologia
Via Donato Creti 12, 40128 Bologna, Italy

Submitted to a special issue of Journal of Climate on the Indian Ocean climate system
April 27, 2005

Corresponding author address: **Hae-Kyung Lee Drbohlav,**
Istituto Nazionale di Geofisical e Vulcanologia
Via Donato Creti 12, 40128 Bologna, Italy
E-mail: hael@bo.ingv.it

ABSTRACT

The Indian Ocean Dipole Mode (IODM) is examined by comparing the characteristics of oceanic and atmospheric circulations, heat budgets, and possible mechanisms of IODM between El Nino and non-El Nino years. ERA-40 reanalysis data, Reynold SST, and ocean analysis from Modular Ocean Model with the assimilation of the temperature profile from World Ocean Dataset 1998 are used to form three-year composites of IODM during El Nino (72, 82, 97) and non-El Nino (61, 67, 94) years. In El Nino years, two off-equatorial, anti-cyclonic circulations develop as a Rossby-wave response to the increased pressure over the Indian Ocean. The resultant winds from easterlies to northeasterlies (from southerlies to southeasterlies) in the northwestern (southeastern) tropical Indian Ocean warms (cools) the mixed layer temperature by inducing an anomalous zonal (meridional and vertical) component in the ocean current that advects the basic-state mixed layer temperature. In non-El Nino years, a monsoon-like flow induces winds from westerlies to southwesterlies (from southerlies to southeasterlies) in the northwestern (southeastern) Indian Ocean. As a result, the cold advection by the anomalous eastward current (northward current) in the northwestern (southeastern) tropical Indian Ocean becomes dominant in non-El Nino years. In addition, the anomalous winds in these regions are the same sign as the climatological monthly mean winds. Hence the anomalous latent and sensible heat fluxes further contribute to the decrease of SST in the northwestern and the southeastern Indian Ocean. Consequently, the cooling of the eastern tropical Indian Ocean rather than the warming of western tropical Indian Ocean becomes the major feature of the IODM during non-El Nino years.

1. Introduction

On interannual timescales the Indian Ocean dipole mode (IODM) is one of the dominant modes in the tropical Indian Ocean. The spatial structure of IODM can be characterized by the negative sea surface temperature anomalies (SSTA) in the southeastern tropical Indian Ocean (ETIO), and the positive SSTA in western tropical Indian Ocean (WTIO). The possible impacts of this spatial structure may cause anomalous precipitation over East Africa, the tropical Indo-Pacific region (Black et al., 2003), and Indian summer Monsoon region (Terray et al., 2003). Especially, the presence of IODM during El Nino years may reduce the influence of El Nino on the Indian summer rainfall (Ashok et al., 2004). In addition, Saji and Yamagata (2003) suggested that the impact of the IODM reaches several remote regions away from the Indian Ocean. They found that a strong correlation between IODM, warm land surface temperature, and reduced rainfall over Europe, northeast Asia, North and South America and South Africa. Therefore, an understanding of IODM is critical for the prediction of the Indian summer monsoon system.

As the role of IODM in climate variability has gained attention in recent years, many efforts have been made to explain the formation of IODM. Gualdi et al. (2003) analyzed the IODM in a coupled model, and suggested a mechanism for the formation of IODM in El Nino years. During the developing phase of an El Nino, positive sea level pressure anomalies are created in the southeastern part of the tropical Indian Ocean. Associated with this anomalous sea level pressure are enhanced southeasterly anomalies, which set up the favorable condition for the IODM (Gualdi et al., 2003).

The role of southeasterlies anomalies on the formation of IODM is further investigated by Li et al. (2003). According to their theory, the presence of both anomalous and mean southeasterlies near the coast of Sumatra in summer enhances the evaporation cooling in this area. The cold SSTA off Sumatra, in turn, increases southeasterly anomalies through a Rossby-wave response. This positive feedback in air-sea interaction is one of the mechanisms that can enhance IODM. Another sustaining mechanism of IODM is proposed by Annamalai et al. (2003). That is, when southeasterlies develop off Sumatra, they induce alongshore upwelling and trigger the IODM, which grows in summer by Bjerknes type feedback.

In spite of these general agreements on the role of southeasterlies, there is a lack of a conclusive theory on the variability of IODM. For example, theories on IODM range from viewing the IODM as a self-sustained independent mode (Saji et al., 1999; Webster et al., 1999) to connecting the IODM with El Nino (e.g., Annamali et al., 2003; Li et al., 2003; Loschnigg et al., 2003). The theory for the independent IODM is supported by statistical evidence (Saji et al., 1999; Yamagata et al., 2002; Behera et al., 2003) and by coupled general circulation model simulations which can simulate IODM without El Nino (Iizuka et al., 2000; Fischer et al., 2005). On the other hand, Li et al. (2003) argued that IODM is a weakly damped oscillator in the absence of strong forcing, such as El Nino. Annamalai et al. (2003) supported this idea by showing that the natural mode of coupled variability of eastern equatorial Indian Ocean is weak on its own but intensifies in spring/early summer, usually when El Nino-like conditions exist in the western Pacific.

The objective of this study is to make a comprehensive comparison between IODM in

association with or without an El Nino. The comparison ranges from atmospheric circulations prior to IODM to the oceanic and atmospheric heat budgets which describe the possible mechanisms of each case of IODM. In order to simplify the diagnostic analysis, a linear estimation is applied so that the interaction between climatological annual cycle (mean) and interannual variability (anomalies) is explicitly identified. Although it is not our interest to overly simplify or emphasis the role of linear processes, this diagnostic analysis can be used to understand the linear mechanisms which supplement existing studies of IODM (Iizuka et al., 2000; Li et al, 2003; Vinayachandran et al., 2002; Annamalai et al., 2003; Loschnigg et al., 2003).

In the next section, a description of data and models is given, followed by explanation of the composite method (Section 3). The formation of IODM during the El Nino years is examined in Section 4. The formation of IODM during non-El Nino years is presented in Section 5. Finally, the main results are summarized in Section 6.

2. Data and models

The data used for the composite of IODM are ERA-40 reanalysis data from European Center for Medium-Range Weather Forecasts (ECMWF), Reynold SST (Reynolds and Smith, 1994) and ocean analysis from Modular Ocean Model (MOM) with the assimilation of the temperature profile of World Ocean Dataset 1998 (WOD98) (Conkright et al., 1998, Masina et al., 2004). The MOM used in this study is the eddy permitted version (Cox., 1984; Rosati and Miyakoda., 1988) with a longitudinal resolution of 0.5^{o}, and a meridional resolution varying

from a minimum of 1/3^{o} between 10^{o}S and 10^{o}N to a maximum 0.5^{o} at the northern boundary. The 31 vertical levels are unevenly spaced with the first 14 levels confined to upper 450m. The model is initialized with the rested ocean, and the climatology of temperature and salinity from winter WOD98. The cloud cover used in the MOM is derived from the climatology cloud cover of the Comprehensive Ocean-Atmosphere Data Set (COADS). The atmospheric forcing variables, such as the air and dew-point temperatures at 2m, the mean sea level pressure, winds at 10m, are taken from the NCEP/NCAR reanalysis project (Kalnay et al. 1996) in order to compute the momentum and heat fluxes interactively with velocity and sea surface temperature (Rosati and Miyajoda, 1988).

The assimilation scheme, used in conjuncture with MOM, consists of the univariate variational optimal interpolation scheme with some changes of parameters from original usage in Masina et al. 2001. The global temperature profile of WOD98 is assimilated into MOM down to the depth of 250m by applying a correction to the forecast temperature field at ever model step. The correction field was created using data from 15 days to either side of the present time step in a statistical objective analysis scheme (Derber and Rosati, 1989). This objective analysis technique is based on the statistical interpolation analysis (Gandin, 1963), which is solved as an equivalent variable problem (Lorec, 1986). The benefit of this assimilation scheme is that the monthly mean fields can be generated with the minimal model adjustment perturbations. The detailed description of MOM and the assimilation procedure can be found in Masina et al. (2001, 2004).

3. Methods

a. Composite of IODM

The monthly means of ERA-40 and MOM are averaged from 1959 to 1999 to produce the climatological annual cycle. The anomaly field is then calculated by subtracting the climatological annual cycle from the monthly means. Years of 1961, 1967, 1972, 1982, 1994, and 1997 are selected to represent the major IODM events (Saji et al., 1999). In those years, except year 1967, the maximum of normalized IODM (IODM/standard deviation of IODM) exceeds two. In years 1972, 1982, and 1997, the IODM accompanies the major El Nino events in which the maximum of normalized Nino3 SSTA exceeds two. Hence, the IODMs of 1972, 1982, and 1997 are averaged to make the composite of IODM during El Nino. For the composite of IODM during non-El Nino years, years 1961, 1967, and 1994 are averaged.

b. Mixed layer equation

In order to understand the variability of the mixed layer temperature, physical processes that control the mixed layer temperature, such as the horizontal advection of mixed layer temperature, the supply of net heat fluxes to the mixed layer and the entrainment of the lower water into the mixed layer need to be examined. Especially, in order to describe the entrainment process, the relative vertical velocity with respect to the varying mixed layer depth has to be estimated. One way to capture this relative vertical velocity is to transform the variables in z coordinate into a new coordinate system where the bottom of the varying mixed layer becomes a constant reference level (Wang et al., 1995). By assuming the consistency of the horizontal velocity and temperature within the mixed layer, and neglecting the shortwave

radiation at the base of the mixed layer and the effect of diffusion, the mixed layer equation can be written as (Wang et al., 1995):

$$\frac{\partial h_{ML}}{\partial t} + \nabla \bullet (h_{ML}\,\mathbf{V_{ML}}) = W_e \qquad (1.a)$$

$$\frac{\partial \mathrm{T_{ML}}}{\partial \mathrm{t}} = -\mathbf{V_{ML}} \bullet \nabla T_{ML} - \frac{W_e}{h_{ML}} \mathrm{H}\ (\mathrm{W_e})(T_{ML} - T_e) + \frac{Q_o}{\rho_o C_w h_{ML}} \qquad (1.b).$$

Here, subscript ML and e imply the mixed layer and entrainment, so that T_{ML} and $\mathbf{V}_{ML}$ denote temperature and horizontal current, vertically averaged over the mixed layer depth, h_{ML}; W_e and T_e are the entrainment velocity at the mixed layer base and temperature of entrained water (Fig. 1); and H (W_e) is a Heaviside function of entrainment velocity. Q_o is the net downward heat flux at the ocean surface; $\rho_o = 10^3$ kg m^{-3} is the density of water; and $C_w = 4.2\mathrm{H}10^7$ Jg^{-1} K^{-1} is the heat capacity of water.

c. Linearized mixed layer equation

The mixed layer equation (1a and 1b) can be linearized, since the variability of the mixed layer anomalies (h'_{ML}) is smaller than that of $\bar{h}_{ML}$ (Figure not shown). The linearized equations are

$$W'_e = \frac{\partial h'_{ML}}{\partial t} + \nabla \bullet (h'_{ML}\,\overline{\mathbf{V}}_{\mathbf{ML}}) + \nabla \bullet (\bar{h}_{ML}\,\mathbf{V}'_{\mathbf{ML}}) \qquad (2.a)$$

$$\frac{\partial \mathrm{T'_{ML}}}{\partial \mathrm{t}} = -\mathbf{V}'_{\mathbf{ML}} \bullet \nabla \bar{T}_{ML} - \overline{\mathbf{V}}_{\mathbf{ML}} \bullet \nabla T'_{ML} - \frac{W'_e(\bar{T}_{ML} - \bar{T}_e)}{\bar{h}_{ML}} - \frac{\overline{W}_e(T'_{ML} - T'_e)}{\bar{h}_{ML}} + \frac{Q'_o}{\rho_o C_w \bar{h}_{ML}} \qquad (2.b).$$

In order to estimate all terms in (2.a) and the first four terms in the rhs of (2.b), the data from the ocean analysis are used. The net heat flux anomalies (Q'_o) in the fifth term of (2.b), however,

is estimated not from ocean analysis but from ERA-40, since the net heat flux (Q'_o) in the ocean analysis is inaccurate. Most importantly, the use of climatological cloud cover in the ocean simulation eliminates the interannual variability in the surface solar radiation. Therefore, the heat fluxes derived from ERA-40 are used to describe the heat flux budget of IODM. In the next section, the analysis on the linear approximation of the net heat flux [fifth term of (2.b)] is followed by the linear estimation of ocean processes [the first four terms on the rhs of (2.b)] during the El Nino years.

4. Formation of IODM in the El Nino years

a. Estimation of heat flux budget from ERA-40, and Reynold SST

According to Saji et al. (1999) the Indian Ocean dipole mode (IODM) is defined as the difference in SST anomaly between the tropical western Indian Ocean (50^oE-70^oE, 10^oS-10^oN) and the tropical southeastern Indian Ocean (90^oE-110^oE, 10^oS-Equator). That is

IODM = SST' (50^oE-70^oE, 10^oS-10^oN) –SST' (90^oE-110^oE, 10^oS to 0^oN) (3).

The composite of IODM from Reynold SST of El Nino years shows a maximum from October to November associated with a warming (cooling) of the western (eastern) Indian Ocean (Fig. 2a). The tendency of IODM ($\frac{\partial\ IODM}{\partial t}$, Fig. 2b) indicates that a persistent forcing of this positive IODM exists from January to October. By using the heat fluxes from ERA-40, the contribution from the surface latent and sensible heat fluxes, and the net surface solar and thermal radiation on the tendency of IODM ($\frac{\partial\ IODM}{\partial t}$) is estimated. That is

Effect of latent and sensible heat fluxes (positive, into ocean) on the formation of dipole mode:

$$\frac{\partial}{\partial t} IODM_{LHF',SHF'} = \left(\frac{LHF'+SHF'}{C_w \rho_o \bar{h}_{ML}}\right)_{WTIO} - \left(\frac{LHF'+SHF'}{C_w \rho_o \bar{h}_{ML}}\right)_{ETIO} \quad (4a)$$

Effect of surface solar radiation and surface thermal radiation (positive, into ocean):

$$\frac{\partial}{\partial t} IODM_{SSR',STR'} = \left(\frac{SSR'+STR'}{C_w \rho_o \bar{h}_{ML}}\right)_{WTIO} - \left(\frac{SSR'+STR'}{C_w \rho_o \bar{h}_{ML}}\right)_{ETIO} \quad (4b)$$

Effect of net heat flux (positive, into ocean) on the formation of dipole mode:

$$\frac{\partial}{\partial t} IODM_{NETHFL'} = \left(\frac{LHF'+SHF'+SSR'+STR'}{C_w \rho_o \bar{h}_{ML}}\right)_{WTIO} - \left(\frac{LHF'+SHF'+SSR'+STR'}{C_w \rho_o \bar{h}_{ML}}\right)_{EIO} \quad (4c).$$

Here, the anomalies of LHF', SHF', SSR', and STR' represent the variability of latent heat flux, sensible heat flux, surface solar radiation, and surface thermal radiation; C_w and ρ_o are the heat capacity and the density of water; subscripts WTIO and ETIO indicate the area average over western tropical Indian Ocean (50°E-70°E, 10°S-10°N) and eastern tropical Indian Ocean (90°E-110°E, 10°S-0°N), respectively. $\bar{h}_{ML}$ denotes the climatology of the monthly mean mixed layer depth derived from the ocean analysis (see next section).

Despite the positive forcing of the latent and sensible heat fluxes in spring and fall (Fig. 2b), the negative forcing of the surface solar and surface thermal radiation hamper the positive effect of latent and sensible heat fluxes (Fig. 2b) throughout the year. As a result, the positive IODM in El Nino years seems to be forced not by the net heat flux but by oceanic processes, such as the horizontal advection and entrainment in (2.b).

b. Estimation of mixed layer heat budget from the ocean analysis

The mixed layer depth (h_{ML}) is defined as a depth whose density difference from the surface is closest to 0.01 kg/m^3 (Jackett and McDougall, 1997). The linearized oceanic processes in (2.b), such as the horizontal advection ($-V'_{ML} \bullet \nabla \bar{T}_{ML}$, $-\bar{V}_{ML} \bullet \nabla T'$) and entrainment [$-\frac{W'_e(\bar{T}_{ML} - \bar{T}_e)}{\bar{h}_{ML}}$, $-\frac{\bar{W}_e(T'_{ML} - T'_e)}{\bar{h}_{ML}}$], are calculated from the ocean analysis. The sum of these linearized terms is then compared with the tendency of IODM from the time series of T'_{ML} in order to access the relative importance of the linearized ocean processes on the formation of IODM (Fig. 3a). Furthermore, the anomalous ocean processes, which include both linear and nonlinear processes, are estimated by 1) calculating the each term of ocean processes (such as horizontal advection and entrainment) from the monthly mean of ocean analysis, 2) Obtain a climatological annual cycle of each term by making an average of each month over 41 years, 3) subtracting the climatological annual cycle of each term from their monthly mean value.

Two local maxima in forcing of IODM, calculated from the time series of T'_{ML}, are found in March and September (Fig. 3a). In those months, the oceanic forcing of IODM also become maxima and comparable to the tendency of IODM. This implies that the linearized ocean processes contribute to the formation of IODM in early spring and late summer. From April to July, however, the forcing of IDOM cannot be explained in terms of oceanic processes. In those months, the nonlinear interaction in the coupled atmosphere-ocean dynamics may become important. Nevertheless, the role of linearized oceanic processes during the formation

of IODM is evident and can be explained by oceanic advection and entrainment in (2.b).

Shown in Figure 3b is the net effect of the linearized oceanic process, as well as the individual contribution to the IODM tendency. The tendency of IODM, induced by the linear approximation, exhibits maxima in both March and September. While the entrainment plays an important role in early spring and late summer, the effect of the meridional advection increases throughout the summer and becomes as large as that of entrainment by September (Fig. 3b).

Although the effect of zonal advection seems to be marginal on the formation of IODM (Fig. 3b), its spatial structure is important to understand the temperature variability of the western Indian Ocean. For example, in August of El Nino years, the anomalous westward current in the northwestern Indian Ocean advects the warm climatological mixed layer temperature of the central tropical Indian Ocean (Fig. 4a). Thus, the advection of mean mixed layer temperature by the anomalous zonal current ($-u'\frac{\partial \overline{T}_{ML}}{\partial x} > 0$) contributes to the increase of T'_{ML} in WTIO (Fig. 4b). Since this positive zonal advection is found not only in the WTIO but also in the ETIO, its contribution on the IODM $[(-u'\frac{\partial \overline{T}_{ML}}{\partial x})_{WTIO} - (-u'\frac{\partial \overline{T}_{ML}}{\partial x})_{ETIO}]$ becomes trivial.

The structure of anomalous meridional advection ($-v'\frac{\partial \overline{T}_{ML}}{\partial y} > 0$) is also examined in Figure 4. When a Rossby wave responds to the cooling of ETIO in September (Fig. 4c), the anomalous northward (southward) current in the eastern (central) part of the southern tropical

Indian Ocean (70°E to 100°E; 10°S to 2°S) advects the cold (warm) climatological mixed layer temperature from the south (north) (Fig. 4c). As a result, the cold (warm) advection becomes dominant in the southeastern (central) Indian Ocean (Fig. 4d). The anti-cyclonic circulation in the northern tropical Indian Ocean (75°E to 95°E; 2°N to 10°N, Fig. 4c) also produces the cold (warm) advection in the northeastern (central) Indian Ocean (Fig. 4d).

It was shown in Figure 3b that the contribution of entrainment on IODM is strongest in March and September. In March, the anomalous entrainment of mean vertical temperature gradient ($-\frac{W'_e(\bar{T}_{ML}-\bar{T}_e)}{\bar{h}_{ML}} < 0$) is negative in the southeastern Indian Ocean, from 92°E to 110°E; 10°S to 4°S (Fig. 5a). The average of this anomalous entrainment over the reference area of ETIO (90°-110°E, 10°S-0°N) is about -0.07° C/month in March. Since the contribution of the entrainment to $\frac{\partial IODM}{\partial t}$ is about 0.15° C/month in March (Fig. 3b), the anomalous entrainment cooling in the ETIO contributes to the half of this value. The other half (0.08 ° C /month) comes from the warming of WTIO by the anomalous detrainment (Fig. 5a). The contribution of this anomalous detrainment is the area averaged value of ($-\frac{W'_e(\bar{T}_{ML}-\bar{T}_e)}{\bar{h}_{ML}}$) between 50°E and 70°E; 10°S and 10°N. Thus, it does not represent the complicated spatial structure of detrainment in the western Indian Ocean. The local convergence (divergence) of anomalous current, especially in the meridional direction, seems to be responsible for the local downwelling (upwelling) and eventually, the detrainment (entrainment) in March.

In September, the spatial structure of anomalous entrainment and detrainment is rather simple (Fig. 5b). Most importantly, there is cooling along the coastline of Sumatra in the ETIO and a general warming of WTIO, except for some areas of small scale. The resultant contribution of the anomalous entrainment (detrainment) in the ETIO (WTIO) is about -0.12 ^{o} C/month (0.06 ^{o} C/month) in September.

It should be noticed that the temperature change associated with detrainment (entrainment) along the coastline of Africa (Sumatra) is smaller than the one predicted by coastal downwelling (upwelling). It is due to the fact that the surge of cold water, induced by the upwelling, does not always penetrate into the mixed layer and affect the mixed layer temperature (2.a). Since, the entrainment velocity in (2.a) is the relative velocity with respect to the mixed layer bottom, which also changes in time ($\frac{\partial h'_{ML}}{\partial t}$), the effect of entrainment and detrainment in the linear approximation seems often smaller than that of upwelling and downwelling.

c. Characteristics of the IODM in El Nino year

Based on the previous analysis of ocean and atmosphere, the characteristics of the IODM during El Nino years are identified. The first feature, which induces the warming along the eastern coast of Africa, is the easterlies and northeasterlies in the region between northern Arabian Sea and the equator (Figs. 6b and 6c). These easterlies and northeasterlies induce a westward component in the ocean current, which advects the climatological warm SST of central Indian Ocean to the western Indian Ocean (Figs. 4a and 4b). As a result, the first sign of the warming in the western Indian Ocean is found in the latitude between 5^{o}S and 15^{o}N.

The second feature of the IODM is the development of the southeasterlies and southerlies in the southeastern Indian Ocean from late spring to fall (Figs. 6b and 6c). The joined force of these anomalies and mean winds along the coast of Sumatra enhances the latent and sensible heat fluxes, cold advection ($-v'_{ML}\frac{\partial \overline{T}_{ML}}{\partial y}<0$), and entrainment in the southeastern Indian Ocean.

The major atmospheric circulation of IODM, such as easterlies and northeasterlies (southerlies and southeasterlies) in the northwestern (southeastern) Indian Ocean seems to be related to the anti-cyclonic circulation, which is located in the northern (southern) Indian Ocean (Figs. 6f and 6g). As the local maximum geopotential anomaly develops poleward of 10^{o}N (10^{o}S) from 50^{o}E to 90^{o}E (from 80^{o}E to 130^{o}E), the accompanying two anti-cyclonic circulations result in the northeasterlies and easterlies over the tropical and the northwestern Indian ocean, and southeasterlies and southerlies in the southeastern Indian Ocean (Figs. 6f and 6g). This suggests that the development of two anti-cyclonic circulations has an effect on the basic characteristics of IODM during El Nino years.

It turns out that these two anti-cyclonic circulations are one of the signatures of El Nino, itself. When the lagged-cross correlation of 850hPa wind and SST anomalies are calculated with respect to NINO3 SSTA (Fig. 7), the development of anti-cyclonic circulation in the northern Indian Ocean (50^{o}E to 100^{o}E; 5^{o}N to 25^{o}N) and southern Indian Ocean (50^{o}E to 100^{o}E; 0^{o}S to 30^{o}S) is detected as early as 6 months before the mature phase of El Nino (Fig. 7b). Associated with these two anti-cyclonic circulations are the easterlies and northeasterlies over the western Tropical Indian Ocean (50^{o}E to 70^{o}E; 10^{o}S to 10^{o}N), and the southerlies and

southeasterlies over the southeastern Indian Ocean (Fig. 7c). The presence of the IODM-like features in the lagged-cross correlation map implies that the development of IODM is, indeed, related to El Nino events.

5. Formation of IODM in the non-El Nino years

It is suggested in the previous sections that the development of the easterlies and northeasterlies (southerlies and southeasterlies) over the western (eastern) Indian Ocean are an important atmospheric condition of IODM in El Nino years. However, the IODM can also be found in non-El Nino years. Thus, it is important to determine if the anti-cyclonic circulation is also presented during non-El Nino years. In this section, the atmospheric condition of IODM during non-El Nino years is compared to that in El Nino years. Furthermore, the oceanic response to the atmospheric circulation of non-El Nino years is also examined.

a. Characteristics of the IODM in non-El Nino years

The characteristics of the IODM in non-El Nino years are different from those in El Nino years in three aspects. First, the dominant easterlies and northeasterlies, often found in the northwestern Indian Ocean during the El Nino years, are absent or weak (Fig. 8). Instead, the westerlies and southwesterlies become dominant in the northwestern Arabian Sea in summer (Fig. 8c). Consistently, the northwestern Indian Ocean no longer experiences the warming (Figs. 8c and 8d), which was the case during El Nino years (Figs. 6c and 6d). This leads to the second difference of non-El Nino years. That is the cooling of ETIO becomes a much more dominant component than the warming of WTIO in IODM during non-El Nino years.

The third difference can be found in the geopotential field in spring (Fig. 8f) and summer (Fig. 8g). While the existence of maximum geopotential anomalies in the southeastern Indian Ocean remains unchanged from El Nino years, the geopotential anomalies along 20^{o}N changes from local maximum in El Nino years (Figs. 6f and 6g) to local minimum in non-El Nino years (Figs. 8f and 8g). Consequently, the northwestern and southeastern Indian Ocean experiences monsoon-like wind anomalies (Fig. 8g), in a sense that the southerlies and southeasterlies in the ETIO, and westerlies and southwesterlies in the northwestern Indian Ocean are prevailing. Thus, the cooling of ETIO is enhanced while the warming of the western Indian Ocean diminishes greatly in non-El Nino years (Fig. 9a).

b. Estimation of heat flux budget from ERA-40 and Reynold SST

In previous section, the difference in the spatial structure of IODM between El Nino and non-El Nino years are described in terms of winds, geopotential, and SST anomalies. These differences affect the atmospheric heat budget, so that the net atmospheric heat flux forcing is now positive though July (Fig. 9b). In the reference area of ETIO (90^{o}E to 110^{o}E; 10^{o}S to 0^{o}N), the anomalous winds of northwesterlies in early part of the year (Fig. 8a) and southerlies and southeasterlies during the rest of the year (Figs. 8b, 8c, and 8d) are the same sign as the climatological monthly mean winds. As a result, the latent and sensible heat flux anomalies in the ETIO increase in non-El Nino years.

c. Estimation of mixed layer heat budget from ocean analysis

The comparison between the tendency of IODM and the effect of linearized ocean processes indicates that the linearized ocean processes before July (after July) underestimate

(overestimate) the forcing of IODM. One of the possible causes of this discrepancy is the increased involvement of atmospheric net heat flux on the formation of IODM until July (Fig. 9b). The impact of linearized ocean processes, on the other hand, is maximum in September (Fig. 10a).

Since the atmospheric winds between non-El Nino years and El Nino years are different, the formation of IODM relies on different oceanic processes. The first difference is the negative effect of entrainment in the early months of the year (Fig. 10b). The northwesterlies along the coast of Sumatra in those months (Fig. 8a) induce the downwelling in the ETIO. The other difference is the increased effect of meridional advection compared to other terms in September (Fig. 10b). It is due to the monsoon-like circulation, which enhances the meridional component of ocean currents, thereby increasing the meridional advection.

6. Summary and discussion

Indian Ocean Dipole Mode (IODM) is examined in a series of composites of ERA-40, Reynold SST, and ocean analysis from a Modular Ocean Model (MOM). The main purpose of this study is not only to understand the formation of IODM, but also to compare the differences of the IODM during El Nino and non-El Nino years.

The differences between El Nino and non-El Nino years are found in the spatial structure of wind and geopotential anomalies. In El Nino years, the development of two off-equatorial, anti-cyclonic circulations is associated with easterlies and northeasterlies (southerlies and southeasterlies) over the northwestern (southeastern) Indian Ocean. One of the

contributing factors of the warm WTIO in El Nino years is these anomalous easterlies and northeasterlies, which induce the ocean currents to advect the warm mean mixed layer of central Indian ocean toward the western Indian Ocean. Meanwhile, the cooling of the southeastern Indian Ocean from spring to late summer is caused by the atmospheric southerlies and southeasterlies, which increase the entrainment and the meridional advection in ETIO.

Different from El Nino years, the geopotential field in non-El Nino years is anti-symmetric with respect to the equator. Thus, the resultant wind anomalies in the northwestern and southeastern Indian Ocean are similar to a monsoon-like circulation. In other words, the westerlies and southwesterlies (southerlies and southeasterlies) are intensified in the northwestern (southeastern) Indian Ocean. Thus, the cold zonal (cold meridional and vertical) advection is enhanced in the northwestern (southeastern) Indian Ocean. In addition, the anomalous winds in those regions are the same sign as the climatological monthly mean winds. Therefore, the anomalous latent and sensible heat fluxes further contribute to the decrease of SST in the northwestern and the southeastern Indian Ocean. Consequently, the cooling of ETIO rather than the warming of WTIO dominates the IODM in non-El Nino years.

The implication of this study is that IODM can be induced by not only El-Nino related winds, but also by the locally enhanced monsoon type circulation. However, IODM under these two types of wind anomalies may evolve into different spatial structures. Especially, the most distinct difference can be found in the SST anomalies in the western Indian Ocean. Since the western Indian Ocean is an important moisture source for the Indian summer monsoon, the different SST anomalies in this region may have varying influence on the Indian Monsoon.

According to Loschnigg et al (2003), the warm SST anomalies of IODM, developed as a part of ENSO-monsoon system and enhanced through the anomalous heat transport, can persist through winter season and contribute to the development of a "strong" monsoon during the following summer. From this context, the weak SST anomalies of western Indian Ocean during non-El Nino year may have less chance of survival and contributing to the following monsoon year. For example, the anomalous summer precipitation (JJA mean) in the Indian Monsoon region (70-100E; 10-25N) is positive in 73, 83, and 98, following the positive IODM of El Nino year (Figure not shown). In years of 62 and 68, however, the precipitation anomalies are negative in spite of the IODM during non-El Nino year (Figure not shown). Since the connection between the warm SST in Indian Ocean and the strong monsoon variability of the following year is essential part of the tropical biennial oscillation (Li et al., 2003; Loschnigg et al.,2003), the IODM during non-El Nino year may not grow into the self-sustained mode of the tropical biennial oscillation.

Acknowledgements

We thank Drs. Simona Masina and Pierluigi Di Pietro for providing the ocean analysis data. This work has been supported by the Italia-USA project.

REFERENCES

Annamalai, H., R. Murtugudde, J. Potemra, S. P. Xie, P. Liu, B. Wang, 2003: Coupled dynamics over the Indian Ocean: spring initiation of the Zonal mode. *Deep-sea Res.*, **50**, 2305-2330.

Ashok, K., Z. Guan, N. H. Saji, and T. Yamagata, 2004: Individual and combined influences of El Nino and the Indian Ocean dipole on the Indian summer monsoon. *J. Climate,* **17***, 3141-3155.*

Black, E., J. Slingo, and K. R. Sperber, 2003: An observational study of the relationship between excessively string short rains in coastal East Africa and Indian Ocean SST. *Mon. Wea. Rev*., **131**, 74-94.

Conkright, M.E., S. Levitus, T. O'Brein, C. Stephen, L. Stathoplos, O. Baranova, J. Antnonv, R. Gelfeld, J. Burney, J. Rochester, C. Forgy, 1998: World Ocean Database 1998. Documentation and quality control. Version 2.1. National Oceanographic Data Center Internal Report 14 OCL/NODC.

Cox, M. D., 1984: A primitive equation, 3-dimensional model of the ocean. *GFDL Ocean Group Tech Rep 1*, pp143.

Derber, J., and A. Rosati, 1989: A global oceanic data assimilation system. *J. Phys Oceanogr.*, **19**, 1333-1347.

Fischer, A., P. Terray, E. Guilyardi, S. Gualdi, and P. Delecluse, 2005: Triggers for the Indian Ocean Dipole/Zonal Mode and links to ENSO in a constrained coupled GCM. *J. climate*, in press.

Gandin, L. S., 1963: Objective Analysis of Meteorological Fields, Gidrometeorologich eskoe Izdatel 'sivo, 242 pp.

Gualdi, S., E. Guilyardi, A. Navarra, and S. Masina, 2003: The interannual variability in the tropical Indian Ocean as simulated by a CGCM. *Clim. Dyn.*, **20**, 567-582.

Iizuka, S., Matsuura, T., and Yamagata, T.,2000: The Indian Ocean SST dipole simulated in a coupled general circulation model. *Geophys. Res. Lett.*, **27**, 3369-3372.

Jackett, D, and McDougall, T., 1997: A neutral density variable for the world's oceans. *J. Phys Oceanogr.*, **27**, 237-263.

Kalnay, E., and Coauthors, 1996: The NCEP/NCAR 40-year Reanalysis Project. *Bull. Amer. Meteor. Soc.*, **77**, 437-471.

Levitus, S., and T. Boyer, 1994: World Ocean Atlas 1994. NOAA Atlas NESDIS, U. S. Department of Commerce, Washington, D. C., 1994.

Lorenc, A. C., 1986: Analysis methods for numerical weather prediction. *Quart. J. Roy. Meteor. Soc.*, **112**, 1177-1194.

Masina, S., N. Pinardi, A., and Navarra, 2001: A global ocean temperature and altimeter data assimilation system for studies of climate variability. *Climate Dynamics*, 1**7**, 687-700.

Masina, S., P. Di Pietro, and A. Navarra, 2004: Interannual to decadal variability of the North Atlantic from an ocean data assimilation system. *Climate Dynamics*, **23**, 531-546.

Li. T, Y. Zhang, E. Lu, and D. Wang, 2002: Relative role of dynamic and thermodynamic

processes in the development of the Indian Ocean dipole: An OGCM diagnosis. *Geophys. Res. Lett.*, **2**9, 2110-2113.

Li, T., B. Wang, C.-P. Chang, and Y. Zhang, 2003: A theory for the Indian Ocean dipole-zonal mode. *J. Atmos. Sci.*, **60**, 2119-2135.

Loschnigg, J., G.. Meehl, P. Webster, J. Arblaster, and G. Compo, 2003: The Asian Monsoon, the Tropical Biennial Oscillation, and the Indian Ocean Zonal Mode in the NCAR CSM. *J. Clim.*, **16**, 1617-1642.

Reynolds, R. W., and T. M. Smith, 1994: Improved global sea surface temperature analyses using optimal interpolation. *J. Clim.*, **7**, 929-948.

Rosati, A., and K. Miyakoda, 1988: A general circulation model for upper ocean simulations. *J. Phys Oceanogr.*, **18**, 1601-1626.

Saji, N. H., B. N. Goswami, P. N. Vinayachandran, and T. Yamagata, 1999: A dipole mode in the tropical Indian Ocean. *Nature*, **401**, 360-363.

Saji, N. H., and T. Yamagata, 2003: Possible impacts of Indian Ocean Dipole mode events on global climate. *Clim. Res*., **25**, 151-169.

Terray, P., P. Delecluse, S. Labattu, and L. Terray, 2003: Sea surface temperature associations with the late Indian summer monsoon. *Clim. Dyn.*, **21**, 593-618.

Vinayachandran, P. N., S. Iizuka, and T. Yamagata, 2002: Indian Ocean dipole mode events in an ocean general circulation model. *Deep-sea Res. II*, **49**, 1573-1596.

Wang, B., T. Li, P. Chang, 1995: An intermediate model of the Tropical Pacific Ocean. *J. Phys Oceanogr.*, **25**, 1599-1616.

Webster, P. J., A. M. Moore, J. P. Loschnigg, R. R., Leben, 1999: Coupled oceanic-atmospheric dynamics in the Indian Ocean during 1997-98. *Nature* **401**, 356-360.

Yamagata, T., Behera, S., Rao, S. A., Guan, Z., Ashok, K., Saji, H., 2002: The Indian Ocean dipole: A physical entity. CLIVAR exchanges **24**, 15-18.

FIGURE CAPTIONS

Figure 1: Schematic diagram of the vertical structure of the ocean. The mixed layer depth (h_{ML}) varies with time and space. The thickness of entrainment sublayer is fixed as 5m.

Figure 2: (a) IODM and SST' in ETIO and WTIO during El Nino years, and (b) tendency of IODM and the contribution from each heat flux.

Figure 3: (a) Tendency of IODM during El Nino year estimated from the time series of T'_{ML} from linear estimation of ocean, and from anomalous ocean processes, which include all ocean dynamics. (b) tendency of IODM during El Nino year estimated from the linearized oceanic processes, and the contribution of each process, such as entrainment, zonal advection and meridional advection.

Figure 4: (a) Mean mixed layer temperature and anomalous zonal current in August, (b) zonal advection induced by the anomalous zonal current acting on the mean mixed layer temperature in August, (c) Mean mixed layer temperature and anomalous meridional current in September, and (d) meridional advection induced by the anomalous meridional current acting on the mean mixed layer temperature in September.

Figure 5: Temperature forcing induced by the anomalous entrainment velocity acting on the mean vertical temperature gradient ($-\frac{W'_e(\overline{T}_{ML}-\overline{T}_e)}{\overline{h}_{ML}}$). (a) March and (b) September of El Nino years.

Figure 6: Spatial patterns of SST' and 850hPa wind anomalies (left panels), and geopotential and 850hPa wind anomalies (right panels) for following monthly averages. (a), (e) January-

February-March mean; (b), (f) April-May-June mean; (c), (g) July-August-September mean; (d),(h) October-November-December mean in El Nino years. 850hPa wind and geopotential anomalies are derived from ERA-40 and Reynold SST is used to calculate SST anoamlies.

Figure 7: Lagged-cross correlation of SST' and 850hPa wind anomalies with respect to NINO3 SSTA. The monthly anomalies from 1959 to 1999 are used for the calculation. 850hPa wind and geopotential anomalies are derived from ERA-40 and Reynold SST is used to calculate SST anomalies.

Figure 8: Same as Figure 6 except for non-El Nino years.

Figure 9: (a) IODM and SST' in ETIO and WTIO during non-El Nino years, and (b) tendency of IODM and the contribution from each heat flux.

Figure 10: (a) Tendency of IODM during non-El Nino year estimated from the time series of $T'_{ML,}$ from linear estimation of ocean, and from anomalous ocean processes, which all ocean dynamics. (b) tendency of IODM during non-El Nino year, estimated from the linearized oceanic processes, and the contribution from each process, such as entrainment, zonal advection and meridional advection.

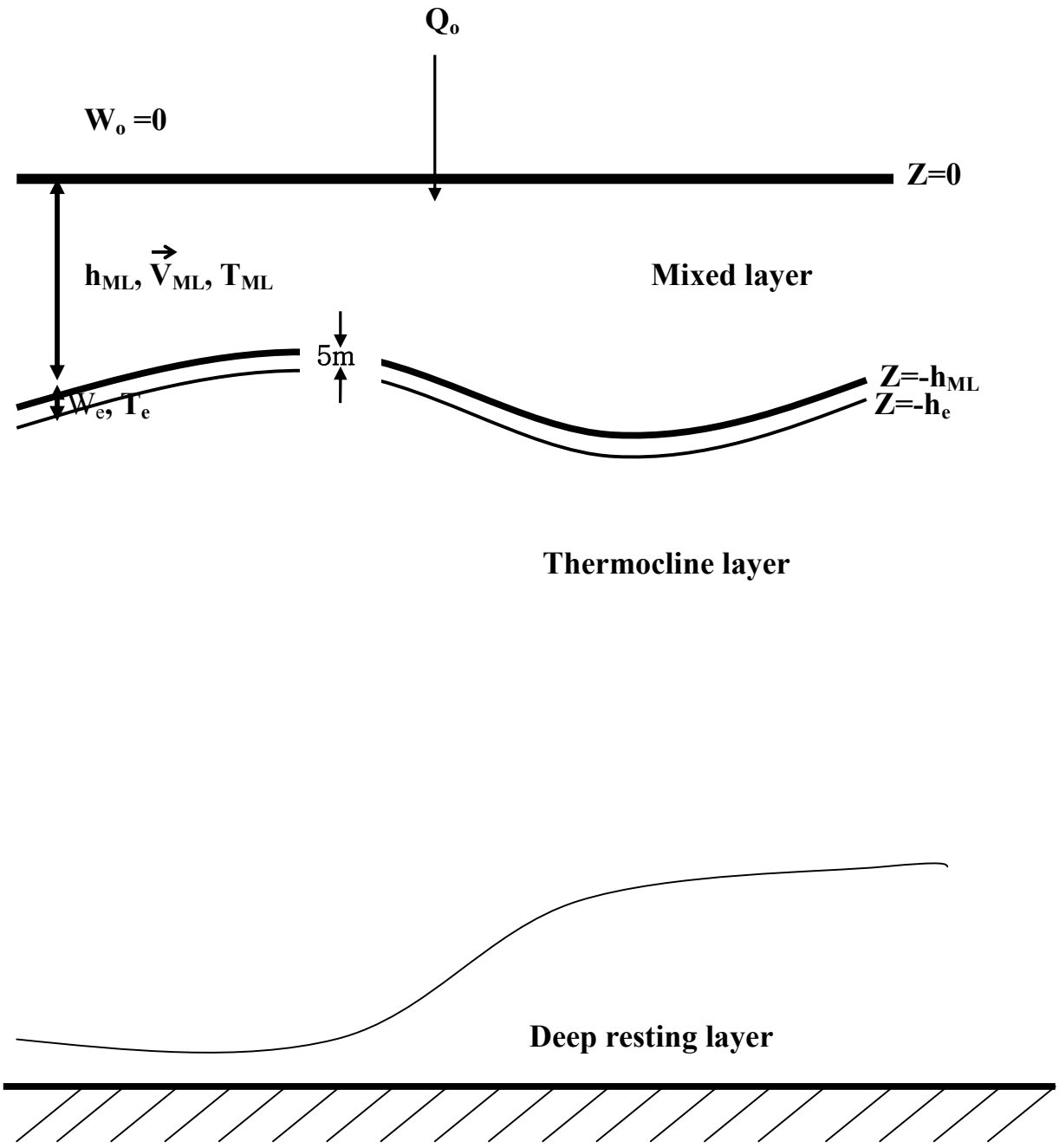

Figure 1: Schematic diagram of the vertical structure of the ocean. The mixed layer depth (h_{ML}) varies with time and space. The thickness of entrainment sublayer is fixed as 5m.

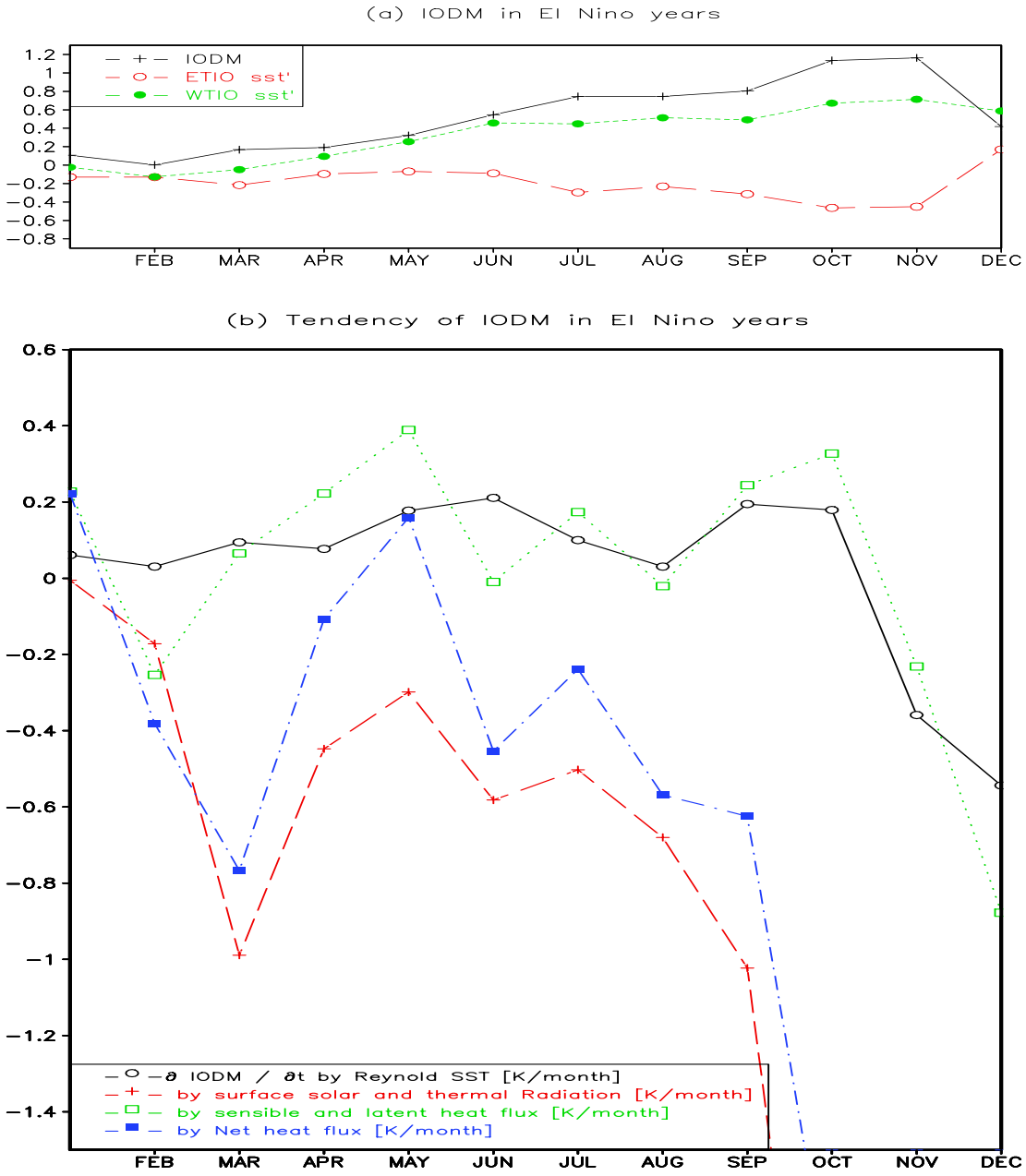

Figure 2: (a) IODM and SST' in ETIO and WTIO during El Nino years, and (b) tendency of IODM and the contribution from each heat flux.

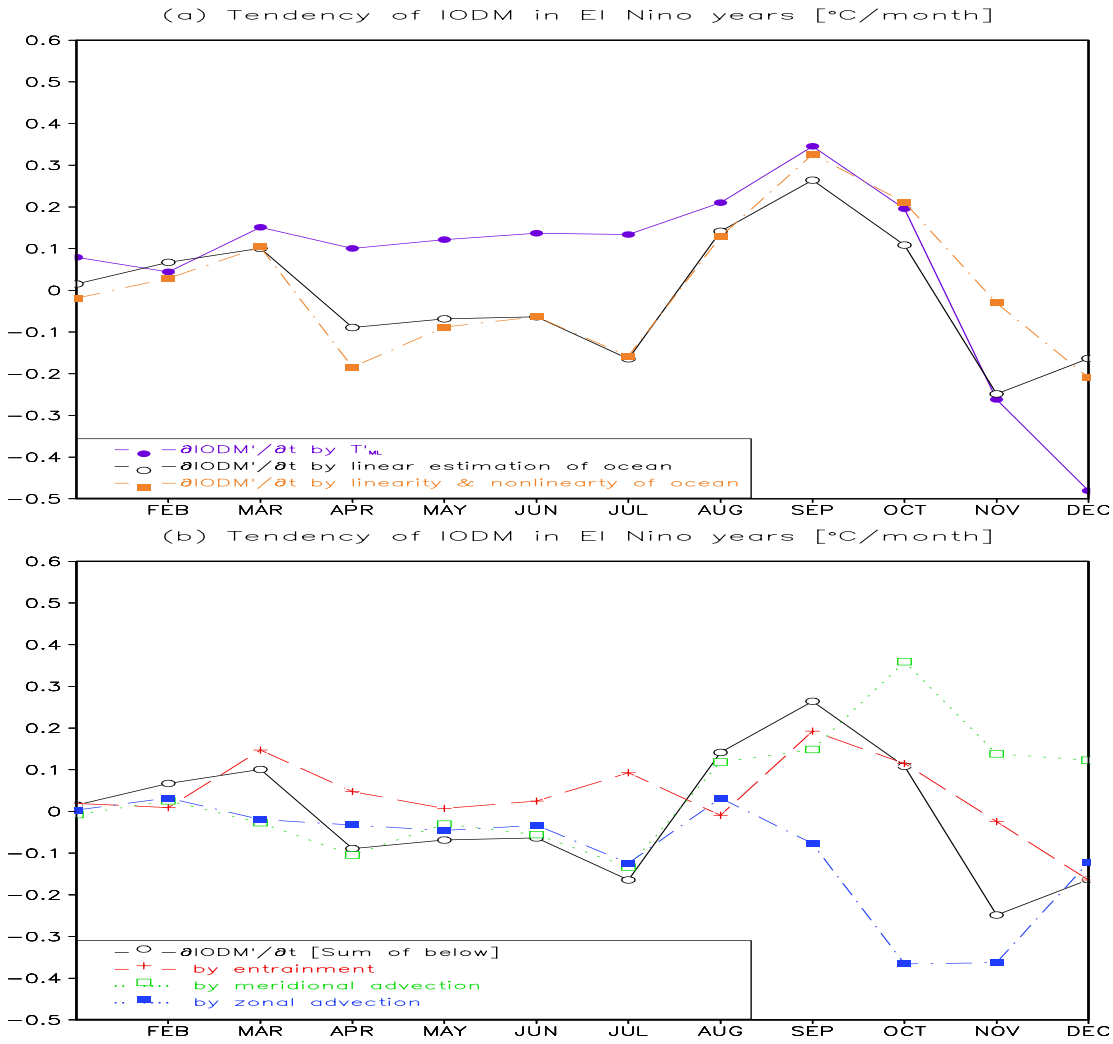

Figure 3: (a) Tendency of IODM during El Nino year estimated from the time series of T'_{ML} from linear estimation of ocean, and from anomalous ocean processes, which include all ocean dynamics. (b) tendency of IODM during El Nino year estimated from the linearized oceanic processes, and the contribution of each process, such as entrainment, zonal advection and meridional advection.

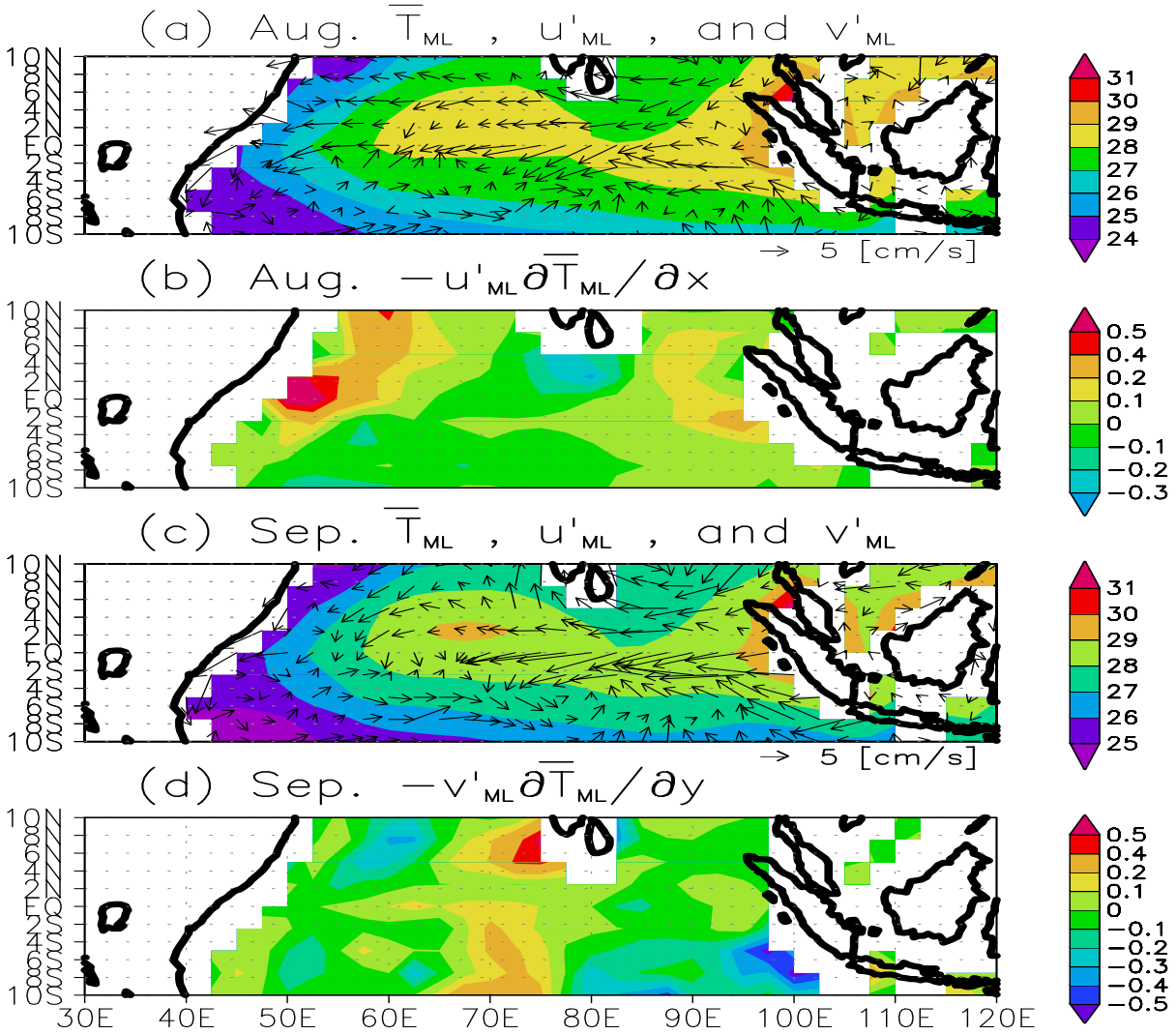

Figure 4: (a) Mean mixed layer temperature and anomalous zonal current in August, (b) zonal advection induced by the anomalous zonal current acting on the mean mixed layer temperature in August, (c) Mean mixed layer temperature and anomalous meridional current in September, and (d) meridional advection induced by the anomalous meridional current acting on the mean mixed layer temperature in September.

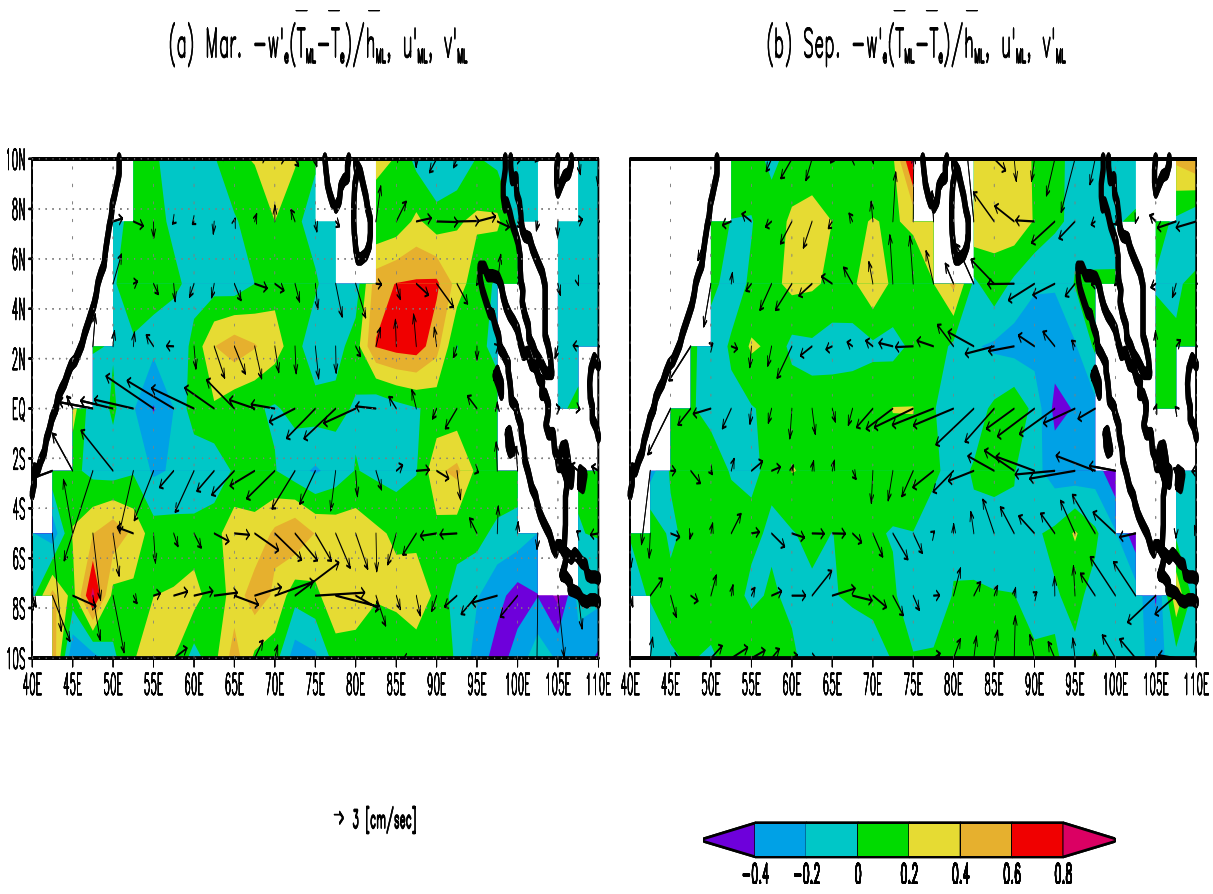

Figure 5: Temperature forcing induced by the anomalous entrainment velocity acting on the mean vertical temperature gradient ($-\frac{W'_e(\bar{T}_{ML}-\bar{T}_e)}{\bar{h}_{ML}}$). (a) March and (b) September of El Nino years.

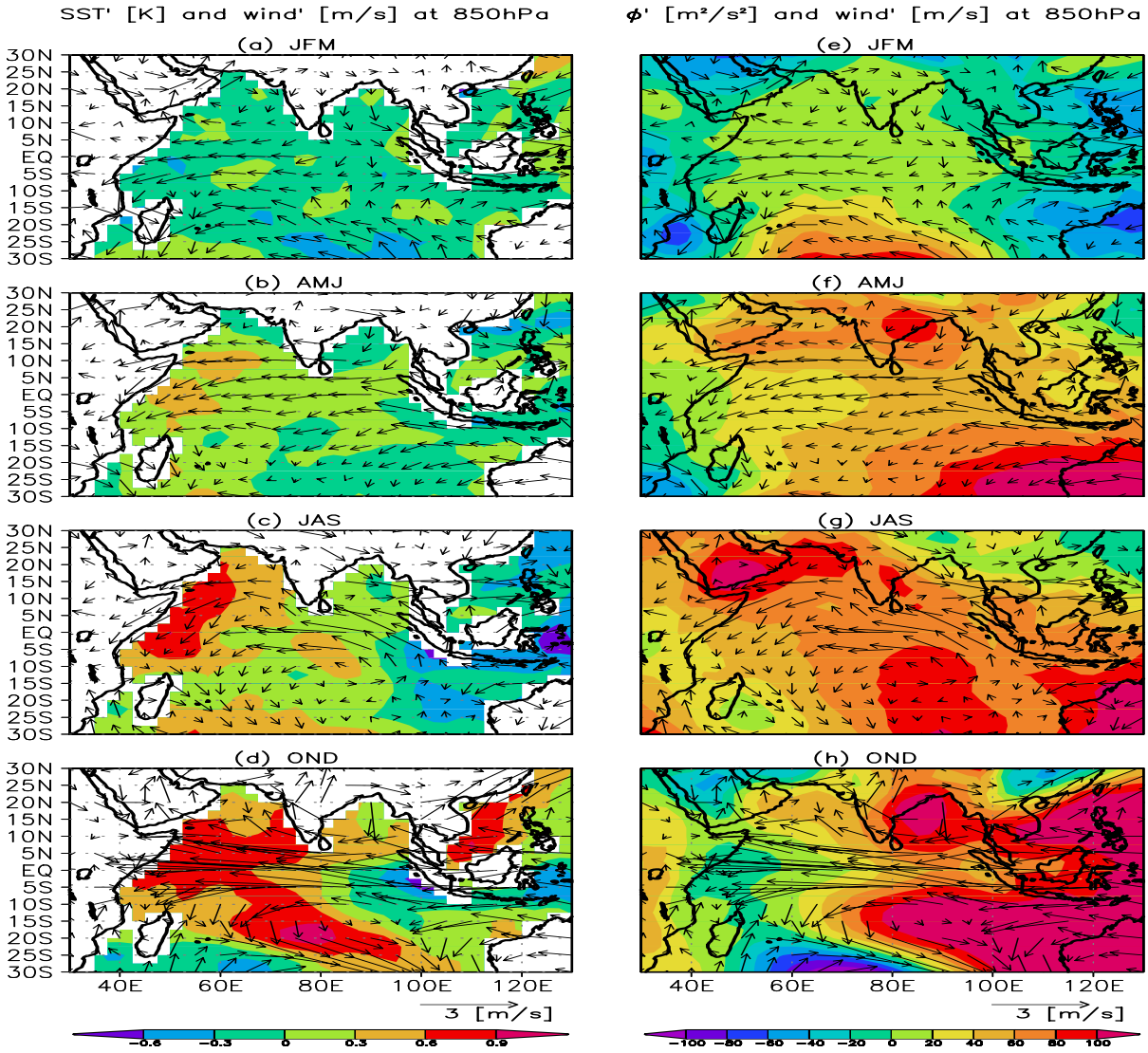

Figure 6: Spatial patterns of SST' and 850hPa wind anomalies (left panels), and geopotential and 850hPa wind anomalies (right panels) for following monthly averages. (a), (e) January-February-March mean; (b), (f) April-May-June mean; (c), (g) July-August-September mean; (d),(h) October-November-December mean in El Nino years. 850hPa wind and geopotential anomalies are derived from ERA-40 and Reynold SST is used to calculate SST anoamlies.

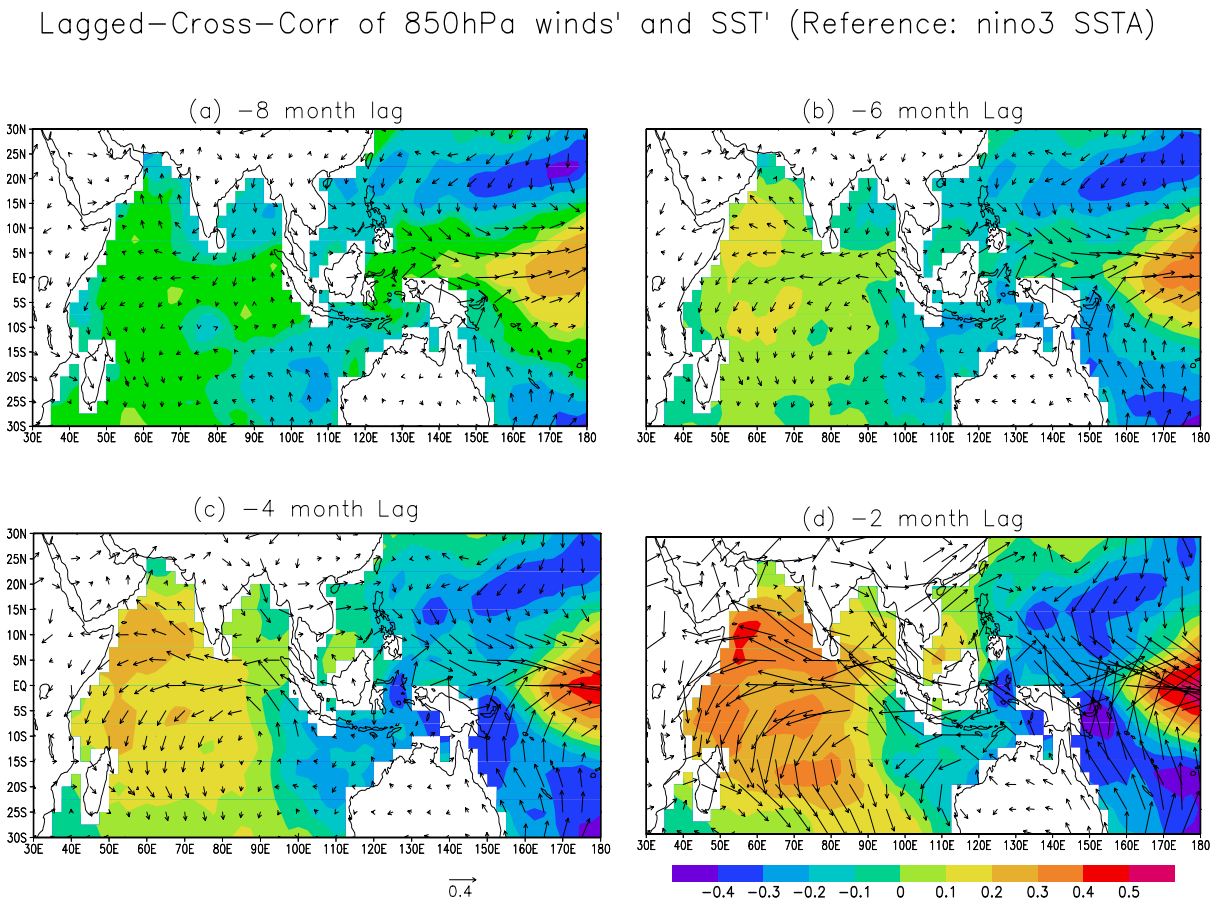

Figure 7: Lagged-cross correlation of SST' and 850hPa wind anomalies with respect to NINO3 SSTA. The monthly anomalies from 1959 to 1999 are used for the calculation. 850hPa wind and geopotential anomalies are derived from ERA-40 and Reynold SST is used to calculate SST anomalies.

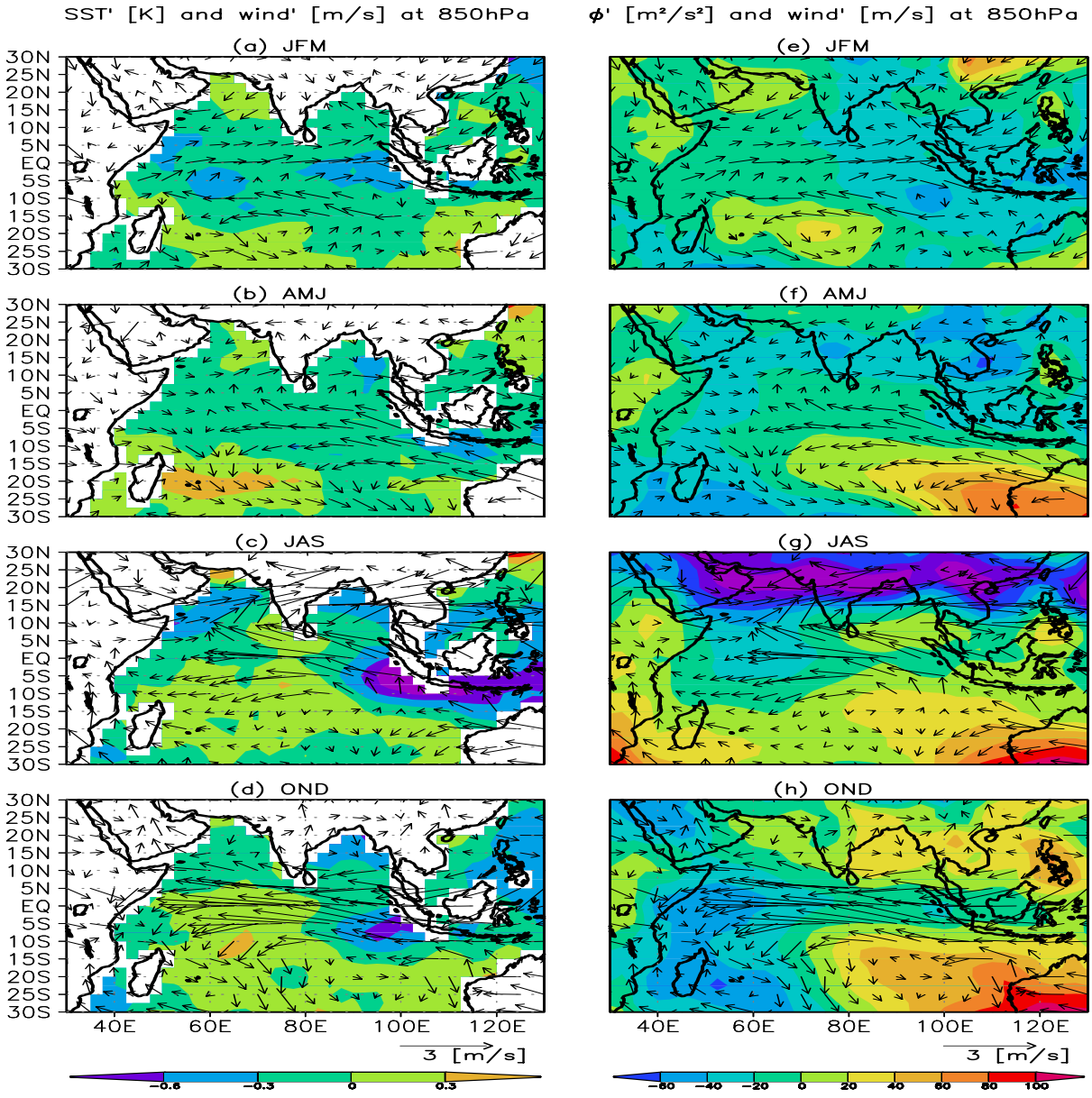

Figure 8: Same as Figure 6 except for non-El Nino years.

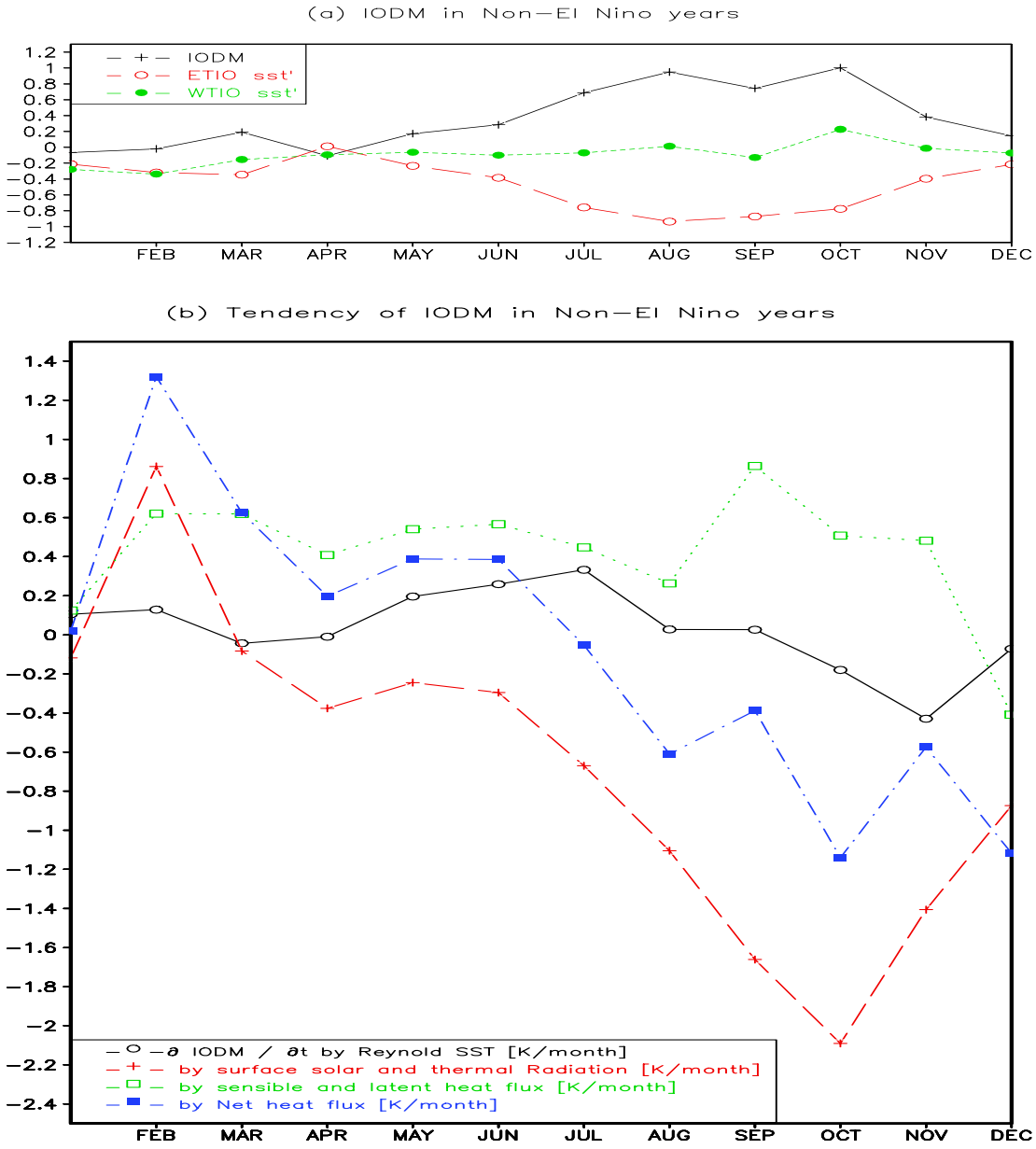

Figure 9: (a) IODM and SST' in ETIO and WTIO during non-El Nino years, and (b) tendency of IODM and the contribution from each heat flux.

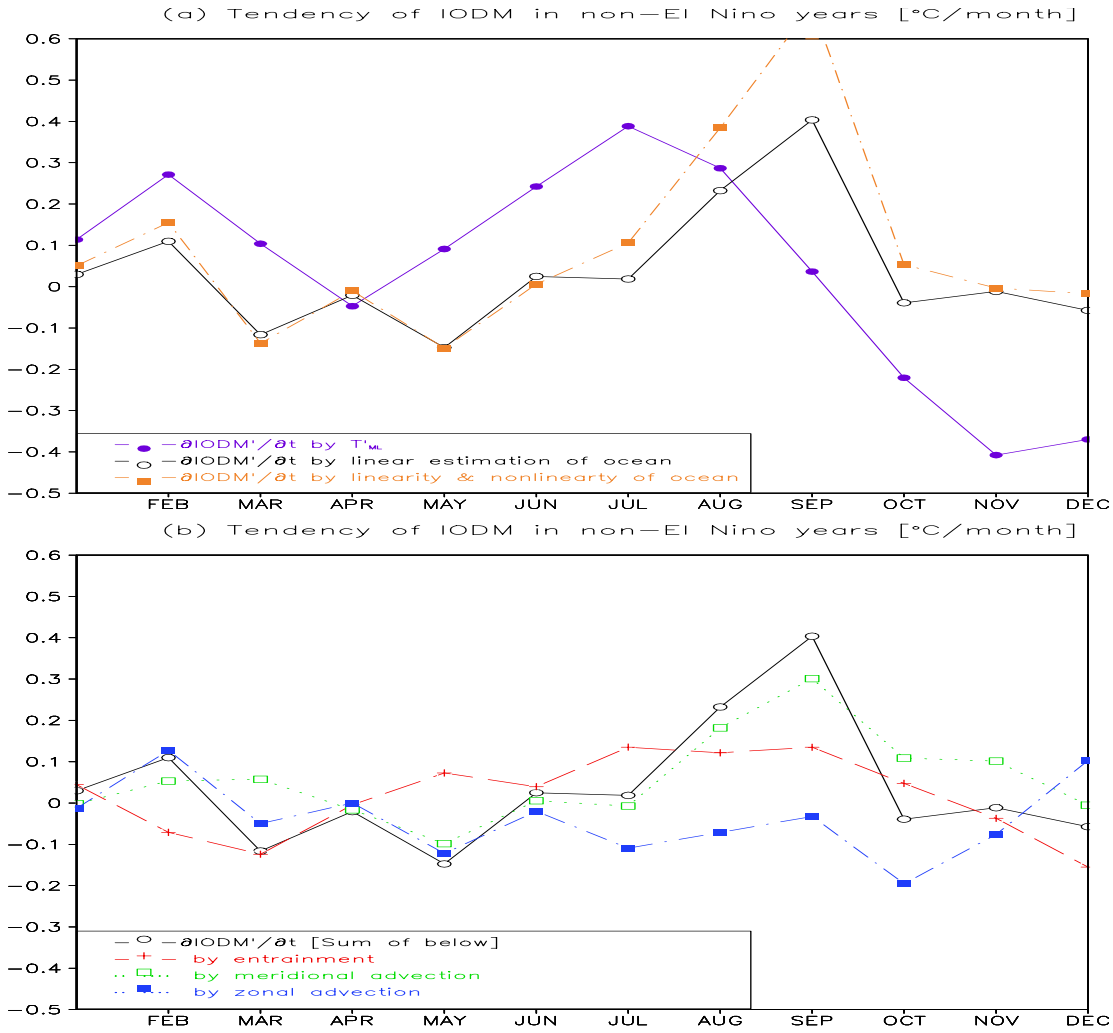

Figure 10: (a) Tendency of IODM during non-El Nino year estimated from the time series of $T'_{ML,}$ from linear estimation of ocean, and from anomalous ocean processes, which all ocean dynamics. (b) tendency of IODM during non-El Nino year, estimated from the linearized oceanic processes, and the contribution from each process, such as entrainment, zonal advection and meridional advection.